Editors' Suggestion

Multiple ferroic orders and toroidal magnetoelectricity in the chiral magnet $BaCoSiO_4$

Xianghan Xu,[1] Fei-Ting Huang,[1] Alemayehu S. Admasu,[1] Marie Kratochvílová,[2,3] Ming-Wen Chu,[4] Je-Geun Park,[2,3,5] and Sang-Wook Cheong[1,*]

[1]*Rutgers Center for Emergent Materials and Department of Physics and Astronomy, Rutgers University, Piscataway, New Jersey 08854, USA*
[2]*Center for Correlated Electron Systems, Institute for Basic Science, Seoul 08826, Korea and Department of Physics and Astronomy, Seoul National University, Seoul 08826, Korea*
[3]*Department of Condensed Matter Physics, Faculty of Mathematics and Physics, Charles University, Ke Karlovu 5, 121 16 Prague 2, Czech Republic*
[4]*Center for Condensed Matter Sciences and Center of Atomic Initiative for New Materials, National Taiwan University, Taipei 106, Taiwan*
[5]*Center for Quantum Materials, Seoul National University, Seoul 08826, Korea*

(Received 17 September 2021; revised 20 April 2022; accepted 21 April 2022; published 10 May 2022)

Discovering ferroic phase transitions and their consequential physical properties is at the core of condensed matter science due to rich physics and tremendous technological promises. $BaCoSiO_4$, a chiral antiferromagnet, belongs to the tetrahedron-based chiral system, and exhibits diverse ferroic orders with coexisting chirality, polarity, trimerization, ferrorotational distortions, and magnetism. However, their mutual couplings remain to be explored. In this work, we used a comprehensive combination of several experimental tools—*in situ* x-ray, transmission electron microscopy, magnetization, and magnetoelectric measurements of single-crystalline $BaCoSiO_4$—to investigate hierarchical phase transitions, their microscopic domain structures, and the resulting magnetoelectricity. We found that two different structural chiralities develop through distinct processes: global homochirality and local heterochirality induced by the ferrorotational distortions on top of existing polarization. In addition, magnetic chirality, with the simultaneous presence of net magnetic moment and magnetic toroidal moment, develops below 3.2 K due to the global chirality, which leads to magnetic field tunable toroidal magnetoelectricity. Thus, $BaCoSiO_4$ exhibits uniquely all four types of ferroic orders and provides an avenue to explore, for example, tunable or dynamic coupling of multiple ferroic degrees of freedom.

DOI: 10.1103/PhysRevB.105.184407

I. INTRODUCTION

Ferroic orders refer to vector order parameters that often break spatial-inversion (SI) or time-reversal (TR) symmetries through phase transitions [1]. The ferroic orders in real materials are perennial topics for rich science and the essence for numerous technological applications. Ferroic orders can be categorized into four groups in terms of even (+) or odd (–) parity under SI and TR operations. Commonly, we have SI^-TR^+ electric polarization and SI^+TR^- magnetization in polar and ferromagnetic materials, respectively. In ferrorotational orders, the local polarizations form a vortexlike head to tail arrangement with an out of plane axial vector, which is invariant under both SI and TR (SI^+TR^+) [2]. The ferrotoroidicity is the magnetic version of ferrorotation by replacing rotating local polarizations with spins and flips under both SI and TR (SI^-TR^-) [3,4]. To date, the understanding of domain configuration and cross coupling of ferrorotation and ferrotoroidicity is still elusive, partially because the material candidates of ferrorotation and ferrotoroidicity are rather limited. Herein, we report that $BaCoSiO_4$ shows ferrorotation and ferrotoroidicity at different temperatures, in addition to structural chirality and polarity. Remarkably, $BaCoSiO_4$ exhibits all of the following: polarization, magnetization, ferrorotation, and ferrotoroidal, corresponding to SI^-TR^+, SI^+TR^-, SI^+TR^+, and SI^-TR^- symmetry breakings, respectively.

Silica (SiO_2) skeleton can hold tetrahedron-based structural chirality; hence, it provides a rich family of materials in which the chiral universality and polymorphic nature can be examined [5]. $BaCoSiO_4$ belongs to one exciting family, the so-called stuffed tridymite with the general formula $ABXO_4$ (A = alkali and alkaline; B and X are tetrahedrally coordinated cations). Unlike quartz with a SiO_4 tetrahedra chain, their corner-shared tetrahedral skeletons build six-membered rings that host the large cation A channels and are packed into a ring-over-ring two-layer structure. Ba-stuffed tridymite derivatives such as $BaMnSiO_4$ [6], $BaFeGaO_4$ [7], $BaAl_2O_4$ [8], $BaMSiO_4$ (M = Co, Mg, Zn) [9], $Ba(Al, Fe)_2O_4$ [10], and $BaZnGeO_4$ [11] have been studied for their rich physical properties, including improper ferroelectricity [12,13], photodielectric effect [14], stripe domain formation [15], luminescence [16], and phonon softening [17], while $BaCoSiO_4$ has received little attention until recently [18]. $BaCoSiO_4$ crystallizes in the noncentrosymmetric $P6_3$ space group with magnetic Co^{2+} ions, and therefore exhibits several ferroic characters such as chirality, polarity, and magnetizations. Furthermore, $BaCoSiO_4$ undergoes a tripling of ab-plane unit cell transition [9], which leads to the cor-

*sangc@physics.rutgers.edu

rugation of the Ba^{2+} layers and tetrahedral tilting and Co trimerization, analogous to the remarkable case of the interplay of the trimerization, magnetism, and polarization in the hexagonal rare-earth manganite family [19], while $BaCoSiO_4$ possesses the additional chiral degree of freedom.

Chirality refers to the situation where an object and its mirror image cannot overlap each other by spatial rotation; i.e., all mirror symmetries are broken in the object. In addition to structural chirality, certain spin arrangements may also develop chirality. We define the concept "magnetic chirality" as a chirality in spin-ordered states (i.e., spin-ordered states with the absence of any mirror symmetry). Magnetic chirality exists in centrosymmetric lattices of frustrated antiferromagnets [20], as well as noncentrosymmetric or chiral lattices with antisymmetric Dzyaloshinskii-Moriya (DM) exchange interactions [21]. Recently, a unique type of magnetic chirality consisting of in-plane toroidal spins plus an out of plane canting was proposed [22], and was, afterwards, experimentally observed in $BaCoSiO_4$. In $BaCoSiO_4$, applying a magnetic field along the c axis can induce "-3 to -1 to 1 to 3" toroidal moment (TM) and c axis canting moment (M_c) transitions, while the magnetic chirality remains invariant [18], which makes it a fascinating system for controllable TM. However, several questions remain not fully understood in $BaCoSiO_4$: what the connection is between the ferrotoroidicity and lattice chirality/polarity, whether the structural domain configuration promises net ferroic quantities, and whether their couplings are experimentally detectable. In this regard, understanding the phase transition routes, revealing ferroic domains, and finding the cross coupling are critical for the subsequent magnetic studies, optical measurements [23,24], and multifunctional applications.

In this paper, applying the laser-diode heated floating zone (LFZ) method, we obtain centimeter-size $BaCoSiO_4$ single crystals, and discuss its domain topology related to chirality, polarity, ferrorotation, and trimerization. The real-space domain evolution involving trimerization and polarity across the structural phase transition has been revealed using *in situ* x-ray structural refinement and *in situ* transmission electron microscopy (TEM). Two kinds of structural chirality have been observed: a global chirality determined by a very high-temperature parent chiral lattice and a local chirality resulting from preexisting polarity plus ferrorotational order. The sample shows a monoglobal chirality which protects a monomagnetic chirality below the ordering temperature of 3.2 K. Therefore, the macroscopic net TM can be efficiently tuned by an external magnetic field, and rich field-tunable magnetoelectric (ME) behaviors have been observed in the single crystal. These findings provide structural hints and multifunctional application potential to the intriguing magnetic interactions [18]. We emphasize that $BaCoSiO_4$ is a unique material that contains ferroic orders covering all four possibilities in terms of the parity of SI and TR.

II. EXPERIMENT

The powder sample of $BaCoSiO_4$ was prepared by a direct solid-state reaction from stoichiometric mixtures of $BaCO_3$, Co_3O_4, and SiO_2 powders (Alfa Aesar, 99.99%). The mixture was calcined at 900 °C in the air for 12 h and then reground, pelletized, and heated at 1200 °C for 20 h and at 1250 °C for 50 h with intermediate grindings to ensure a total reaction. At the end of each sintering, a quenching process, i.e., taking the sample out of the furnace quickly at the target temperature, is desired for the correct phase, since $BaCoSiO_4$ tends to decompose at intermediate temperatures. The resulting pure powder sample is supposed to be bright blue in color. Slow cooling can cause significant decomposition, visually indicated by the sample color turning purple. Large single crystals were grown using a laser-diode heated floating zone (LFZ) technique. The optimal growth conditions were growth speed of 2–4 mm/h, atmospheric airflow of $0.1\,l\,min^{-1}$, and counter-rotation of the feed and seed rods at 15 and 30 rpm, respectively. The large temperature gradient of LFZ guarantees a rapid cooling on as-grown crystal, which suppresses the decomposition at intermediate temperature. We tried to grow it by conventional optical floating zone, but the crystal quality was poor. Attempts to tailor the ionic ordering by annealing the as-grown crystal at temperature range 850 °C to 1200 °C also failed due to significant crystal decomposition.

The *in situ* high-temperature x-ray diffraction was performed on both powder and single-crystal samples of $BaCoSiO_4$. The powder was characterized using the high-resolution x-ray diffractometer Bruker XRD D8 Discover with Cu $K\alpha$ radiation. The diffractometer is equipped with a high-temperature chamber HTK 1200N for measurements in an ambient atmosphere up to 1200 °C. Structural parameters were refined by the Rietveld method using the FULLPROF program [25]. Differential scanning calorimetry (DSC) data were taken on SETSYS Evolution TGA-DTA/DSC SETARAM with the DSC-800 °C rod in He atmosphere, each sample (typical mass ∼50 mg) being measured once upon warming and cooling at the rate of 10 °C/min up to 780 °C. Standard alumina crucibles with a diameter of 0.5 cm and a height of 0.8 cm were used. Transition temperatures were determined as the onset of the observed peaks upon warming.

Specimens for TEM studies were prepared by mechanical polishing, followed by Ar ion milling. Domain structures were studied using a JEOL-2010F transmission electron microscope equipped with a 14-bit charge-coupled device (CCD) array detector. The *in situ* heating TEM experiment was carried out using a JEOL-2000FX TEM with a high-temperature specimen holder. All images are raw data.

For pyroelectric and magnetoelectric measurements, a $BaCoSiO_4$ single crystal was oriented by the Laue method and cut and mechanically polished into an ab-plane plate and an ac-plane plate both with thickness of 20 μm. The electrodes were made of silver epoxy. The crystals were cooled down to 2 K with DC 50.5 kV/cm (applied by a Keithley 617 electrometer) and 2 T poling E, H fields in a PPMS-9. All isothermal ME measurements were performed by 200 Oe/s magnetic field sweeping at 2 K. The magnetic field and heating rate of all pyroelectric measurements were 1.5 T and 5 K/min. A Keithley 617 electrometer collected current signals while ε was measured in PPMS-9 with oscillating electric fields using a Quadtech 7600 LCR meter at 1 V and 44 kHz. All presented figures are made by raw data.

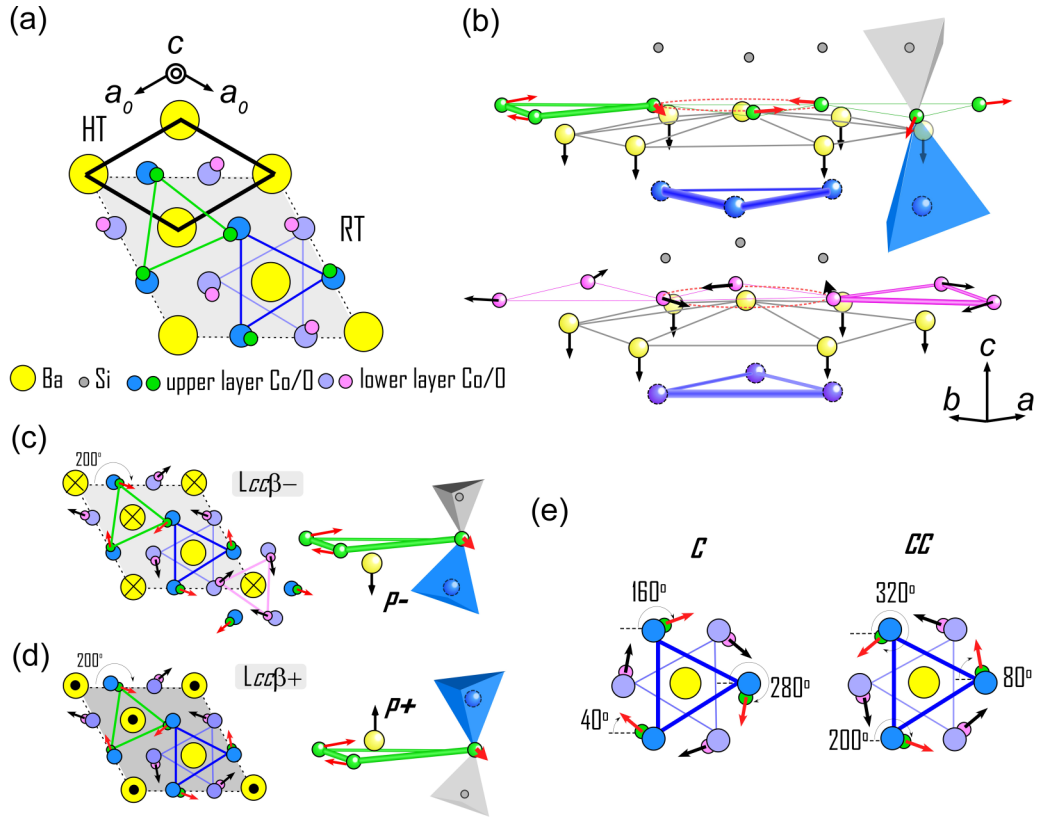

FIG. 1. Room-temperature crystal structure of $BaCoSiO_4$. (a) The thick solid line and dashed line represent the high-temperature ($a_0 \times a_0$) and the room-temperature ($\sqrt{3}a_0 \times \sqrt{3}a_0$) unit cells, respectively. The triangles with green/blue/purple bars correspond to Co/O trimers. (b) Three-dimensional crystallographic structure of $BaCoSiO_4$, showing double-layer lattices of SiO_4 and CoO_4 tetrahedra. The large/yellow and small/gray spheres represent the Ba and Si ions. The blue/green spheres display the upper CoO_4 layer and purple/pink ones display the lower CoO_4 layers. The tetrahedral tilting leads to the Ba ion displacements and the trimerization of Co and O ions. (c) The projection of $Lcc\beta-$ state. The Lcc unit stands for left chiral with counterclockwise oxygen distortions. $\alpha/\beta/\gamma$ antiphase relations correspond to 80°, 200°, and 320° oxygen in-plane rotations. The Ba^{2+} downward distortion arises from the up-pointing apices of CoO_4 tetrahedron (blue) and the squeezing O trimer (green bar) from the top. The large yellow circles show the positions of Ba ions, with crosses or dots indicating displacement into or out of the plane within one unit cell. The "–" sign means a net Ba^{2+} downward polar distortion along the c axis. (d) The projection of the $Lcc\beta+$ state with a net Ba^{2+} upward distortion. (e) Clockwise (c) and counterclockwise (cc) ferrorotational distortion of bridging oxygens and their angles, which are closely related with antiphase domains.

III. RESULTS AND DISCUSSION

A. Structural characterization

$BaCoSiO_4$, the room-temperature (RT) phase ($P6_3$) ($a = 9.1203$ Å and $c = 8.6643$ Å), exhibits diverse ferroic orders including chirality, polarity, trimerization, ferrorotational distortion, and magnetism. Figure 1(b) depicts two-layered $Co^{2+}O_4$ (blue) and $Si^{4+}O_4$ (gray) tetrahedra, linked by their oxygen vertices to form triangular lattice layers. The tetrahedra are tilted to induce the Co^{2+} trimerization in each Co layer (the triangles with blue and purple bars) and the trimerization of those bridging oxygens in each O layer (the triangles with green and pink bars). These distortions result in a $\sqrt{3} \times \sqrt{3}$-type superstructure from the high-temperature (HT) phase as shown in Fig. 1(a). A finite polarization exists along the c axis due to the displacement of the Co^{2+} and Si^{4+} ions from the center of the tetrahedra and the shifts of Ba^{2+} ions. Figure 1(c) as the projected view of Fig. 1(b) illustrates the arrangement of $Si^{4+}O_4$ (D, down-pointing apices) and $Co^{2+}O_4$ (U, up-pointing apices) tetrahedra accompanied by the low distortion of two-thirds of the Ba ions (yellow balls) and the nondistortion of one-third of the Ba ions in a down-down-none configuration. A reversed $Co^{2+}O_4$(U)/$Si^{4+}O_4$(D) tetrahedra will lead to Ba^{2+} with an up-up-none configuration, as shown in Fig. 1(d).

In addition, we note that the projected displacement map of those bridging oxygens reveals a circular rotational pattern surrounding the nondistorted Ba ion [small green and pink spheres around yellow spheres in Fig. 1(e)]. Consequently, two propellerlike orientations of those bridging oxygens, termed ferrorotational distortion, are denoted as c (clockwise) and cc (counterclockwise). The ferrorotational order, whose order parameter is an axial vector invariant under both time-reversal and spatial-inversion operations, has only been realized recently in $RbFe(MoO_4)_2$ [2]. Those ferroic orders lead to 24 possible domain configurations of the RT phase as summarized in Fig. 2, combining left (L) and right (R) chirality preserved from the HT phase, + or − polarity (up- or down-orientation of the polar displacement), c or cc ferrorotation of the bridging oxygens, and three possible translation variants of trimerization (α, β, and γ represent different origins for the trimerization). For example, the domain depicted

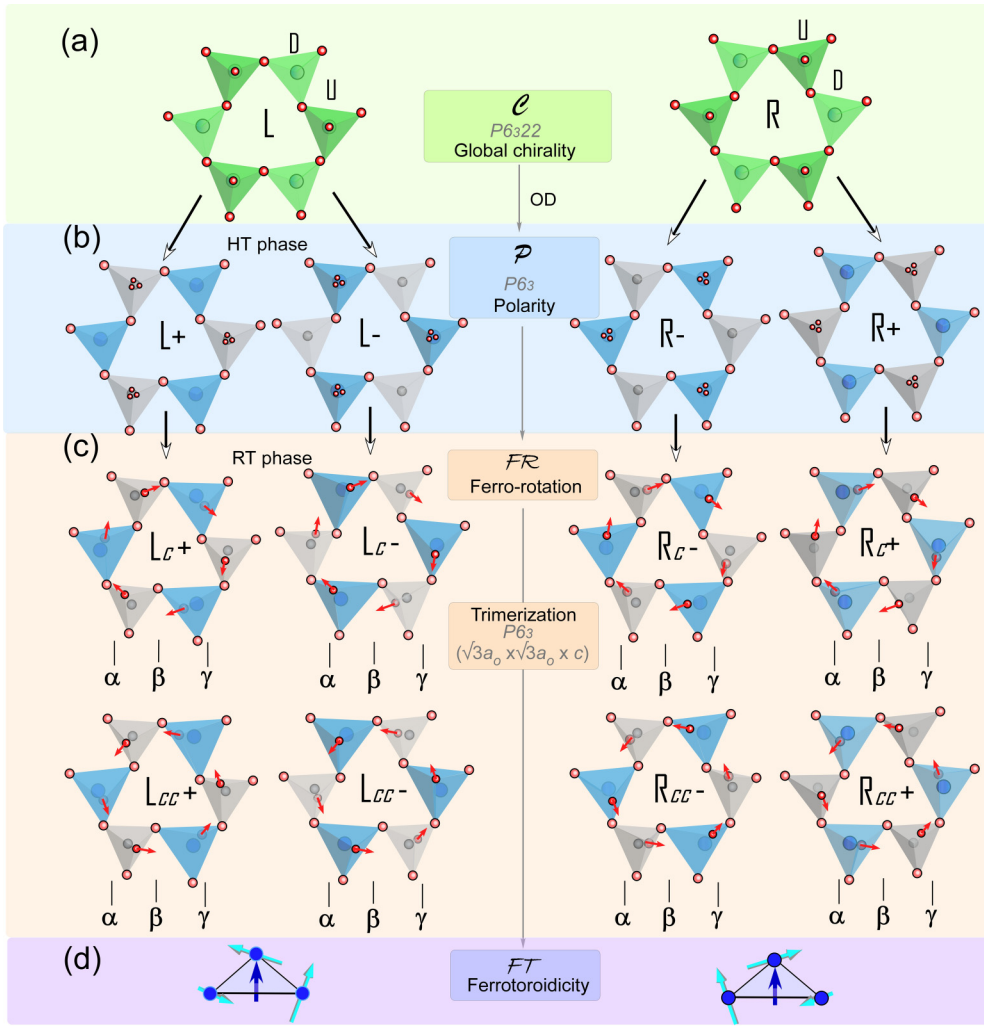

FIG. 2. Phase transition hierarchy of $BaCoSiO_4$. (a) The parent chiral phase ($P6_322$), showing the left-handedness of DUDUDU and the right-handedness of UDUDUD six-membered rings of tetrahedra points alternating up (U) and down (D). (b) A Co^{2+}/Si^{4+} order-disorder (OD) transition leads to the breaking of in-plane twofold rotation and the HT phase with a chiral and polar symmetry ($P6_3$). The gray, blue, and red spheres represent the Co, Si, and O ions. The apical O atoms are shifted off the threefold axes and split over three equivalent positions to eliminate linear Si-O-Co linkages. Signs + or − indicate the net up or down polar distortion related to down and up CoO_4 tetrahedral geometries. (c) The 24 domain configurations of the RT phase as a result of chirality, polarity, trimerization ($\alpha/\beta/\gamma$ antiphase displacements), and ferrorotation (c and cc ferrorotational distortion of bridging oxygens). L$c\alpha+$ represents a left-chiral unit in a clockwise oxygen distortion with α-type antiphase domain and an upward polar distortion. (d) Below 3.2 K, rotating Co^{2+} spins in each triangle form a toroidal moment pointing c. This magnetic structure with a canting magnetization M_c is also chiral, and this magnetic chirality is determined by the parent chiral lattice described in (a).

in Fig. 1(c) is labeled as L$cc\beta-$, in which L$cc\beta$ represents a left-chiral unit in a counterclockwise oxygen distortion with β-type antiphase domain while the sign "+" or "−" indicates the net up- or down-orientation of the Ba^{2+} ions. Six symmetry-equivalent domains of the Lcc unit are shown in Fig. S1 in the Supplemental Material [26].

B. Chirality

First, we start $BaCoSiO_4$ on the point of chirality. Figure 2(a) illustrates two six-membered rings of $BaCoSiO_4$ tetrahedra with DUDUDU or UDUDUD orientations, in which up (U) and down (D) stand for the pointing direction of the tetrahedral apices along the c axis. A mirror operation relates two orientations that preserve the chiral tetrahedral unit, thus labeled as left chiral (L) and right chiral (R). The absolute chirality determination must be confirmed. It appears the chirality comes with the Co^{2+}/Si^{4+} site mixing [Fig. 2(a)], a paraelectric structure of space group $P6_322$ develops with a linear tetrahedral string oriented along the c axis since the up and down tetrahedral apices remain at the high-symmetric position. The crystallographic structure is already chiral even above the Co^{2+}/Si^{4+} order-disorder (OD) process as illustrated in Fig. 2(b), and, herein we name its chiral origin as parent chiral lattice. With the settling down of Co^{2+}/Si^{4+} site ordering from cooling, CoO_4 and SiO_4 tetrahedral tilts occur due to sizable ionic size differences, resulting in the broken in-plane twofold axes and a lower symmetry (space group

$P6_3$). We find that the parent lattice chirality, i.e., the global chirality, is preserved in the following room-temperature (RT) phase.

Indeed, Fig. 3(a) shows a single chiral domain of our $BaCoSiO_4$ single crystal under transmission-polarized optical microscopy (t-POM) for the light propagating along the chiral c axis. The size of the observed chiral domains is on a centimeter-size scale. The single chiral domain is robust and does not change when a polycrystalline seed is applied during the crystal growth or postannealing below the decomposition temperature (∼850 °C). Namely, the structural chirality is already fixed during the crystal growth, and it governs the handedness and the robustness of the single chiral domain observed here. In this regard, we narrow it down to 12 domain configurations in our $BaCoSiO_4$ crystals (Fig. 2).

C. Trimerization and ferrorotational orders

Next, a clear structural transition takes place around 530 °C, identified using differential scanning calorimetry (DSC) shown in Figs. S2(a) and S2(b) [26]. *In situ* powder XRD measurements in Fig. S2(c) show the temperature dependence of the lattice parameters derived from the Rietveld refined plots of $BaCoSiO_4$ in the temperature region between RT and 800 °C. The transition temperature from XRD seems slightly lower than that from DSC, while the small discrepancy is within the DSC-measurement error ∼5 °C. The HT phase is free from superlattice reflections, while the RT phase shows $a = \sqrt{3}a_0 (a_0 \sim 5.29\,\text{Å})$ superstructure within the hexagonal plane. The transition is accompanied by an increase of the lattice parameter c by ∼1.4% (from 8.6936 Å at 500 °C to 8.8148 Å at 700 °C) upon warming. Figure 1 displays the refined chiral and polar RT structure that is consistent with the literature [9], and the powder XRD refinement data of the RT and HT phases are displayed in Figs. 4(a) and 4(b).

Upon increasing temperature, the evolution of peaks (002) and (101) (at $2\theta = 20.1^\circ$ and 21.8°) in the HT powder XRD data is evident [Fig. 4(c)]. Several structures ($BaAl_2O_4$, $BaZnGeO_4$, $BaGa_2O_4$) [8,27,28] were tested to describe the HT phase described by the space group $P6_322$ (#182), and the (002) and (101) peaks can be reasonably described by the β-$BaGa_2O_4$ structure with a single tetrahedral site of disordered Co^{2+}/Si^{4+}. The apical oxygen O_2 $6h$ (x, $2x$, $\frac{1}{4}$) connecting tetrahedra are also shifted off the threefold axes and split over three equivalent positions from the high-symmetric position $2d$ ($\frac{1}{3}$, $\frac{2}{3}$, $\frac{1}{4}$) to avoid linear linkages. A significant splitting of the bridging oxygen over three statistically occupied sites implies the local ordering of Co^{2+}/Si^{4+}. Refinement using the $P6_3$ space group with ordered Co^{2+}/Si^{4+} did not result in any improvement; however, considering the same R factors within the error margin, significant bond length difference (Si-O: 1.62 Å and Co-O: 1.97 Å), and the relatively large values of the U_{eq} parameters, the refined result with $P6_322$ symmetry of disordered Co^{2+}/Si^{4+} is not contrary to the possibility that $P6_322$ symmetry serves as an average symmetry only.

On the other hand, the tripling unit cell structural phase transition at 530 °C is confirmed. The bridging oxygen distortion comes in so that the trimerization and ferrorotation are closely related with those bridging oxygens, as depicted in Figs. 1(b)–1(c). Based on the XRD results alone, we cannot decide whether the structural transition at 530 °C is a trimerization/ferrorotational transition, i.e., $P6_3$ ($a_0 \times a_0$) to $P6_3$ ($\sqrt{3}a_0 \times \sqrt{3}a_0$) or a polar coupled phase transition, i.e., $P6_322$ ($a_0 \times a_0$) to $P6_3(\sqrt{3}a_0 \times \sqrt{3}a_0)$.

D. Polarity

To gain insight into the structural change at 530 °C, the microstructure observations were performed using dark-field (DF) TEM, in which domain contrasts of dynamical diffraction can occur based on the Friedel pair breaking in a noncentrosymmetric structure [29,30]. Specifically, we can examine the polar domains using a suitable reflection with at least a component along the polarization direction, i.e., c axis in addition to three types of antiphase domains (α, β, and γ) from the trimerization. In a polar phase transition coupled with trimerization/ferrorotational transition, one may expect a similar cloverleaf pattern observed in the hexagonal rare-earth manganite due to the interlocked polar and structural antiphase boundaries (APBs), otherwise, not. Figure 3(b) shows a DFTEM image taken $g = (4\bar{3}2)$ along $[\bar{1}02]$, tilted from [001], by 27° to incorporate the c axis (polar) component. We observe three antiphase domains emerging from one point instead of six domains with alternating dark and light contrast. Numerous nanoscale speckles indicated with white arrows in Fig. 3(b) distribute within each antiphase domain. The DFTEM image clearly shows the decoupled nanoscale lateral polar domains and the structural antiphase domains, whose size can be about a few hundred nanometers. The correlation of nanoscale lateral polar domains is long along the c axis, as shown in Fig. 3(c) along [110].

The microstructures revealed by DFTEM support a trimerization/ferrorotational transition at 530 °C and the scenario of disordered $P6_322$ symmetry being an average HT phase. The local polar regions also indicate a short-range positional order of Co^{2+}/Si^{4+} tetrahedra in the entire $BaCoSiO_4$ single crystal at RT, determined by Co^{2+}/Si^{4+} order-disorder process at a temperature far above 530 °C. The phase transition hierarchy shown in Fig. 2 reveals that the paraelectric to polar transition coincides with the Co^{2+}/Si^{4+} order-disorder (OD) process and then follows the trimerization/ferrorotational transition at 530 °C. Indeed, the picture of local polar regions is consistent with the necessary quenching process during the polycrystalline preparation and the rapid growth rate in the LFZ method to stabilize the Co^{2+} ion. The polarization cannot be flipped at room temperature, indicating pyroelectricity, which can be understood as the obstacle of the migration of Co^{2+}/Si^{4+} cations in the ferroelectric reversal path.

E. Trimerization and domain evolution

The presence of antiphase boundaries (APBs), as shown in Fig. 3(b), is the consequence of trimerization, resulting in three possible translation variants. The APBs, visible as narrow dark curved lines, tend to form a network of triple junctions named Z_3, as there are plenty at RT, and start to disappear above 540 °C in Fig. 5. Figure 3(e) illustrates a pair of Z_3 vortex-antivortex of $Lcc\alpha-$, $Lcc\beta-$, and $Lcc\gamma-$

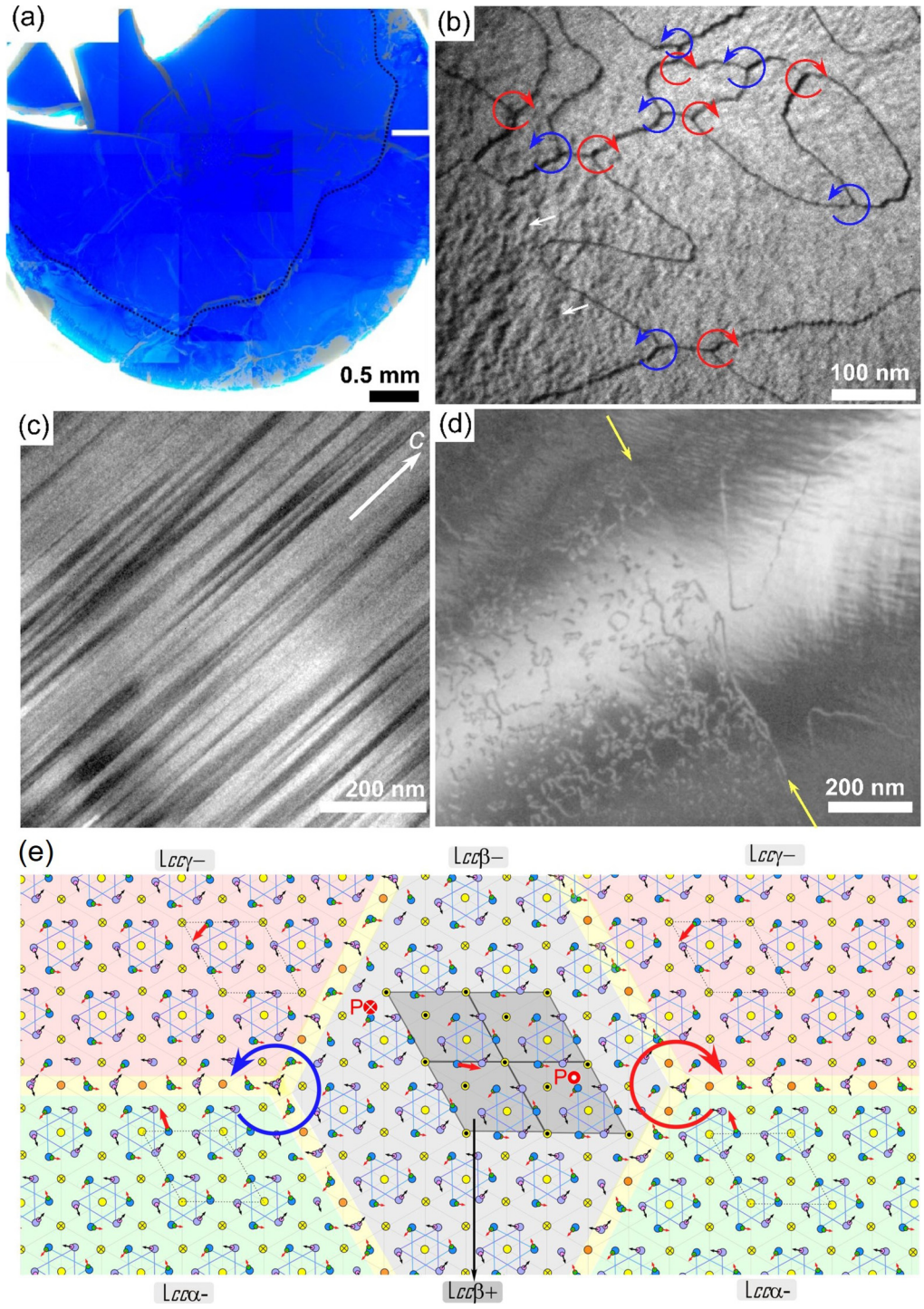

FIG. 3. Four ferroic orders in $BaCoSiO_4$. (a) Polished cross section of a LFZ crystal boule of $BaCoSiO_4$ with (001) surface with two mosaic domains and a single chiral domain; its natural color is deep blue under a transmission mode Axio-Imager optical microscope (t-POM). (b) In-plane DFTEM showing antiphase boundaries as dark lines. Three symmetry-equivalent antiphase domains exist because of trimerization. Triple-point junctions are marked in blue and red arrows. Many nanometer-sized dark speckles appear inside antiphase domains as indicated by white arrows, indicating nanoscale lateral polar domains. (c) Side view DFTEM of polar domains elongating along the c axis. Dark and bright regions corresponding to two different polar domains appear by selecting the $(2\bar{2}2)$ spot along [110]. (d) In-plane DFTEM of ferrorotational domains demonstrates the discontinuation of trimerization at the ferrorotational boundary indicated by yellow arrows. (e) The schematic of a pair of Z_3 vortex-antivortex by the 120° apical oxygen rotations (red arrows) across antiphase boundaries. The blue/purple triangles correspond to the top and bottom Co trimers, and the arrows on the atoms depict the in-plane oxygen rotation. The yellow dots and crosses represent the upward and downward distortions of Ba^{2+} ions. Big central red and blue arrows indicate the vorticities obtained by counting the rotating directions in the clockwise direction. A portion of the L$cc\beta+$ region exists in the central L$cc\beta-$ region due to local Co^{2+}/Si^{4+} ordering.

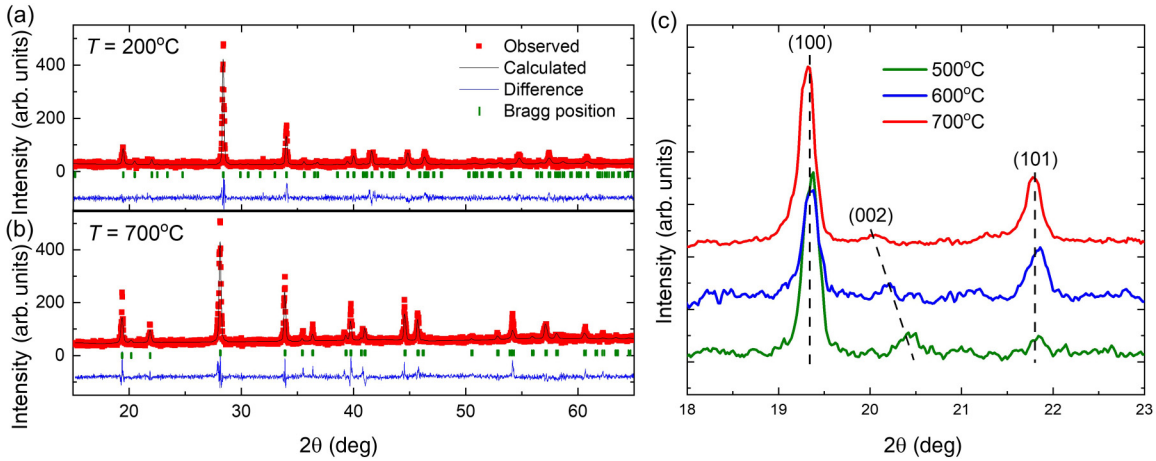

FIG. 4. Powder XRD refinement data of RT and HT structures. (a) The refinement data at 200 °C. The observed, calculated, and difference profiles are shown by red squares, black line, and blue line, respectively. The green bars indicate the positions of the Bragg reflections. (b) The refinement at 700 °C. Symbols have the same meanings as in (a). (c) The evolution of Bragg reflections (002) and (101) from 500 °C to 700 °C.

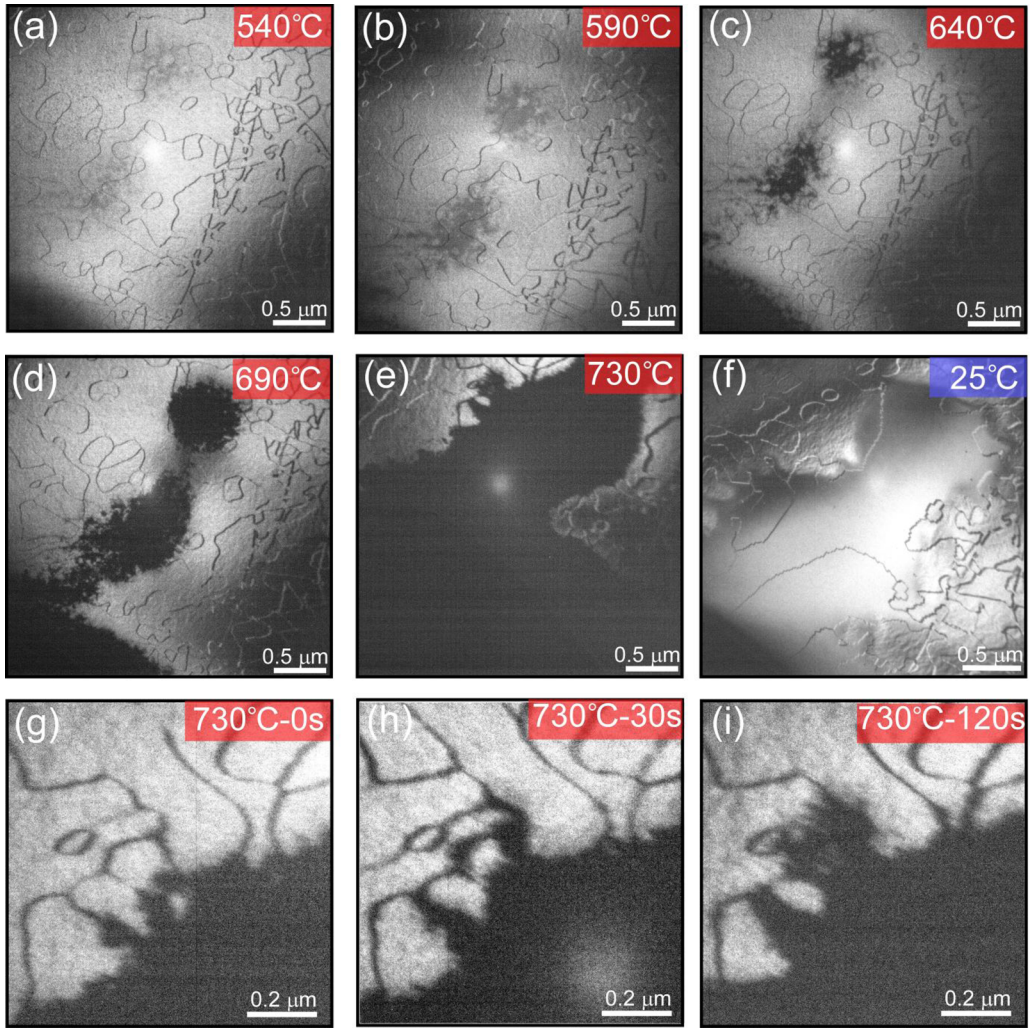

FIG. 5. Dark-field TEM images of $BaCoSiO_4$ at different temperatures. (a)–(e) Black regions, the nucleated HT phase, are observed above 530 °C. Bright regions with dark lines of antiphase boundaries are the residual RT phase. (f) A different Z_3 pattern forms after a warming-cooling cycle. (g)–(i) The HT phase is evolved from those dark lines, APBs, during *in situ* heating.

domains, where α, β, and γ represent different origins for the trimerization. An oxygen distortion vector [bold red arrows in Fig. 3(e)] rotates every 120° around a vortex core. In a clockwise cycle, an increment in an angle of $+2\pi$ is counted as a vortex and a decrement of -2π as an antivortex. Yellow atomically sharp structural domain walls and two vortex cores surround the central L$cc\beta-$ domain. Local polar up regions (L$cc\beta+$) exist within the central polar down region (L$cc\beta-$) in the presence of nanoscale Co^{2+}/Si^{4+} ionic ordering. Since only the discontinuation of trimerization occurs at the APBs, it leads to a local lattice compensation at those APBs, i.e., the HT phase.

We study the domain evolutions in a warming-up process through the trimerization/ferrorotational transition at 530 °C. This can be inspected using *in situ* heating DFTEM by selecting the superlattice peaks. The domain evolution at elevated temperatures is captured by incrementally raising the temperature. The coexistence of HT and RT phases can be identified during the *in situ* heating, manifesting as dark and light areas, as shown in Figs. 4(a)–4(e). The light areas exhibit the Z_3 network while there is no feature within the dark areas. Continuing to raise the temperature leads to the vanishing of light areas as the $\sqrt{3}a_0 \times \sqrt{3}a_0$-type superlattice peaks disappear. Figures 4(g)–4(i) show clearly that the HT phase is evolved from those dark lines of APBs that correspond to the growth of the HT phase from those APBs of the RT phase. Figure 5(f) demonstrates the reversible process and a completely different Z_3 pattern after further cooling the specimen temperature to below 530 °C.

Note that the 530 °C transition is also the ferrorotational transition ascribed to the *c* or *cc* displacements of the bridging oxygens. As shown in Fig. 1(d), defining this *cc* in-plane rotating angle to be 200°, symmetry-equivalent structures are obtained for rotating angles of 320° and 80°. We likewise obtain 40°, 160°, and 280° for clockwise in-plane rotating angles. Because of the noninteger relation of those *c* and *cc* in-plane rotating angles, we observe the interruption of the Z_3 network at ferrorotational domain walls as shown in Fig. 3(d). Experimentally, a continuous Z_3 network tends to extend over a large area, indicating a larger scale of ferrorotational domains. It can be understood in terms of symmetry. Above the 530 °C transition, the apical O atoms are split over three equivalent positions [Fig. 2(b)] while the threefold symmetry along the *c* axis is maintained. A condensation to multiple *c* and *cc* ferrorotation domains below the transition will undoubtedly break the threefold symmetry and unfavor it. The lateral domain sizes among four ferroic orders of our $BaCoSiO_4$ crystals are domains of chirality (cm size) > ferrorotation (a few hundred μm) > antiphase (a few μm to a few hundred nm) > polarity (tens of nm laterally).

F. Magnetic chirality and magnetoelectric effect

The magnetoelectric (ME) effect can occur in ferroic materials [31]. The first experimental demonstration of magnetoelectricity was performed on Cr_2O_3, in which electric field induced magnetization and magnetic field induced polarization with linear ME coefficient $\alpha_{zz} = 4.13\,\mathrm{ps\,m^{-1}}$ were observed [32–35]. Subsequently, researchers have discovered various ME compounds such as $TbPO_4$ [36], $Fe_2Mo_3O_8$ [37], and Ni_3TeO_6 [38]. Unlike the above materials showing induced magnetization/polarization parallel to the applied field, it was found that the magnetic toroidicity allows the control of magnetization/polarization by fields perpendicular to them [4], as illustrated in materials such as $LiNiPO_4$ [39], $LiCoPO_4$ [40], $LiFeSi_2O_6$ [41], and $Ga_{2-x}Fe_xO_3$ [42]. Besides those compounds, the exploration of TM induced ME materials is very limited to date. Ni_3TeO_6 has a polar and chiral structure, but the magnetic ground state is collinear without toroidicity or magnetic chirality. Therefore, $BaCoSiO_4$ is a great candidate showing both structural and magnetic chirality, which could lead to a robust and field-tunable ME effect induced by TM.

We note two-step structural chirality in $BaCoSiO_4$: (1) the monoglobal chirality fixed by the very high-temperature parent chiral lattice, and (2) the various local chiralities induced by the ferrorotation with existing polarization, i.e., nanoscale lateral polar domains. Though ferrorotation, which does not break space inversion, does not induce optical activity, it has symmetry operation similarity (SOS) with a structural chirality in the presence of polarization [24,43]. Then, the structural chirality can generate magnetic chirality through DM interactions. If the global structural chirality determines magnetic chirality, the whole crystal shall show a monoferrotoroidal domain when applying magnetic field along the *c* axis, and TM induced ME effects should be observed [4], otherwise, not.

We prepared *ab*-plane and *ac*-plane single-crystalline plates and tested their ME properties by applying magnetic fields along various directions and collecting the induced current signal. The setup of electrodes and external magnetic field directions is shown in Figs. 6(a) and 6(b) for *ab*-plane and *ac*-plane plates, respectively. For the *ab*-plane crystal, the pyroelectric current shows a much clearer anomaly at the Néel temperature ~3.2 K (from the $\chi(T)$ in Fig. S2(d) [26]) when applying magnetic field along the *c* axis rather than the *a* axis (Fig. S3(a) [26]). Consistently, at 2 K, magnetic field sweeping along the *c* axis induces a large ME current signal up to 2 pA (Fig. S3(c) [26]) and a polarization up to 90 $\mu C/m^2$ [Fig. 6(c) upper panel]. The anomaly and tripled slope in the polarization curve at $H_c = \pm 1.2$ T agree with the reported field-induced "1–3" M_c transitions [18]. Therefore, in the *ab*-plane crystal, the dominated ME effect happens when both P and H are parallel to the *c* axis. This behavior is not surprising considering $BaCoSiO_4$ is a noncentrosymmetric hexagonal system with polarization and net magnetization along the *c* axis [37,38]. As shown in Fig. S4 [26], the fitting of $P_c(H_c)$ by $P_c = C + \alpha H_c + \beta {H_c}^2$ yields $\alpha = 5.42(2)$ ps/m, $\beta = 2.01(6) \times 10^{-18}$ s/A for the high-field region (1.5–7 T), and $\alpha = 6.13(7)$ ps/m, $\beta = -1.96(4) \times 10^{-18}$ s/A for the low-field region (0–0.9 T). The linear term has the same order of magnitude with the reported $\alpha = 4.13$ ps/m in Cr_2O_3, and the quadratic term is comparable with the reported $\beta = 2.959 \times 10^{-18}$ s/A in another noncentrosymmetric antiferromagnet $Co_2Mo_3O_8$ [44]. This coexisting of the linear term and the quadratic term ME effect has also been observed in the high-field region of noncentrosymmetric hexagonal magnet $Ni_2Mo_3O_8$ [45]. In $Ni_2Mo_3O_8$, it has been suggested that the low-field AFM state has a symmetry that does not allow the linear term, while

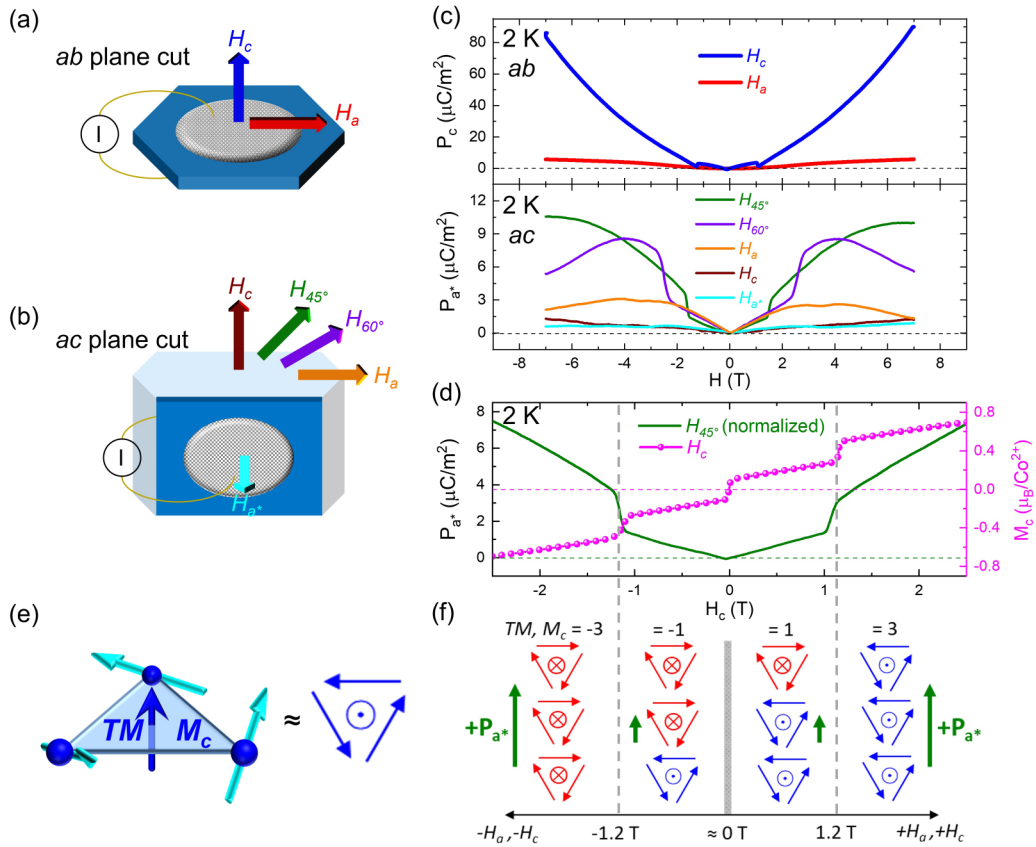

FIG. 6. Magnetoelectric effect of $BaCoSiO_4$. (a), (b) Schematics of electrodes and magnetic field directions on *ab*-plane (a) and *ac*-plane (b) single crystals. (c) Magnetoelectric polarization as a function of applied fields measured on *ab*-plane (upper panel) and *ac*-plane (lower panel) single crystals at 2 K with magnetic field along various orientations shown in legends. The color of each curve corresponds to the field indicated with the same color of arrows as in (a), (b). (d) The 2 K isothermal $M_c(H_c)$ data (magenta), which is from Ref. [18], and magnetoelectric polarization as a function of fields pointing 45° in between *c* and *a* (olive). The field is normalized by dividing $\sqrt{2}$ to make *c* component H_c as the *x* axis. (e) Schematics of the magnetic structure of one Co sublattice. Blue spheres represent Co ions, and cyan and blue arrows show spins and resulting TM and M_c, respectively. (f) A schematic showing the "–3 to −1 to 1 to 3" TM and M_c change with applied field along *c*. Polarizations (olive arrows) along a^* are induced with the presence of the magnetic field component along *a*. The narrow shaded area near zero field denotes the tiny hysteresis regime.

field-induced ferromagnetic moments in high fields could contribute to a linear term. It should be noticed that the magnetic space group of $BaCoSiO_4$ and high-field $Ni_2Mo_3O_8$ both contain *c*-rotation operation ***6***. Since the space inversion and time reversal are all broken by polar lattices and ferromagnetic moments in ***6***, it allows both linear and quadratic ME effects along the *c* axis. Our results show that the linear term α remains almost invariant below and above the 1–3 transition, while the quadratic term β flips its sign, which suggests that the quadratic term depends more on the net magnetic moments while the linear term stays almost unaffected. In addition, although a significant ME effect is observed in $P_c(H_c)$, the dielectric constant ε (T) along the *c* axis does not show clear anomaly at T_N at various magnetic fields along the *c* axis (Figs. S5(c) and S5(d) [26]).

More interesting behaviors come with the *ac*-plane crystal. As shown in Fig. S3(b) [26], among H parallel to *a* (orange), *c* (wine), and a^* (cyan) axes, the pyroelectric current when $H \| a$ shows the clearest peak at the Néel temperature of 3.2 K. Accordingly, the observed polarization at 2 K with $H \| a$ sweeping is much larger than the $H \| a^*$ and $H \| c$ cases [Fig. 6(c) lower panel]. For a TM along the *c* axis, the induced ME effect requires $H \perp c$, $P \perp c$, and $H \perp P$, which is precisely consistent with the P, H assignment in which the significant ME effect was detected on the *ac*-plane crystal. Therefore, we can conclude that the observed off-diagonal ME effect ($P \| a^*$, $H \| a$) originates from a magnetic toroidicity contribution. In the low-field region (–2 to 2 T), the induced polarization is nearly linear to the applied field, and it decreases when the field is larger than 4 T. The reason for this behavior could be that the large in-plane magnetic field tends to coalign spins through a spin-flop transition and suppress the TM. Consistently, we also observed the disappearance of the magnetodielectric effect at magnetic field larger than 3 T, as shown in Figs. S5(a) and S5(b) [26].

Note that even if the magnetic field was applied along the *a* axis, practically, there could always exist a tiny *c* component of the magnetic field due to misalignment. This tiny *c* component could flip the magnetization, especially considering the reported coercive field of $BaCoSiO_4$ M_c is extremely small, which is only around 50 Oe [18]. To investigate this possibility, a TM induced ME measurement within a low field range

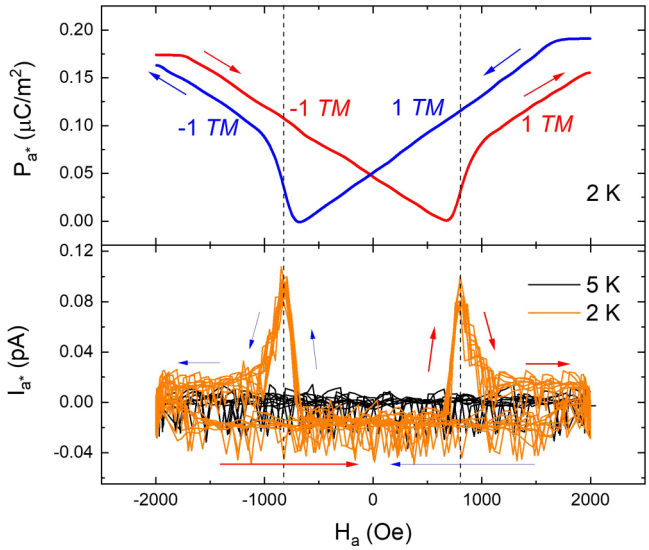

FIG. 7. The low field (–2000 to 2000 Oe) region of $I_{a^*}(H_a)$ (lower panel) and $P_{a^*}(H_a)$ (upper panel). In the lower panel, orange and black lines represent magnetoelectric current $I_{a^*}(H_a)$ at 2 K (below transition) and 5 K (above transition), respectively. The red and blue arrows mark the ascending and descending magnetic field H_a sweeping loop. In the upper panel, the red and blue curves show the polarization P_{a^*} as a function of ascending and descending magnetic field H_a, respectively.

−2000 to 2000 Oe was performed and displayed in Fig. 7. Clear peaks at around ±800 Oe and "butterfly" hysteresis behavior confirm the flipping of M_c by a tiny c component of applied field, as well as the ferroic nature of TM. From the reported coercive field of M_c 50 Oe, the misalignment of the magnetic field can be estimated to be 3.5°, which is reasonably small enough. We notice that the induced polarization P_{a^*} is markedly linear to applied magnetic field H_a within −2000 to 800 Oe (ascending) and 2000 to −800 Oe (descending) ranges, with a linear ME coefficient $\alpha = 1.03(4)$ ps/m.

We have learned that applying a magnetic field along the c axis can triple the TM as well. However, detecting the corresponding ME effect requires a magnetic field component perpendicular to the c axis. Therefore, to reach the ME effect with tripled TM, the applied H should contain both c and a components. The olive and violet curves in the lower panel of Fig. 6(c) display ME current and polarization measured in such a way that the magnetic field orients 45° and 60° to the c axis, respectively. Consistently, "1 to 3" TM transitions are observed around 1.6 T [expected to be 1.2/cos(45°) T] for $H_{45}{}^\circ$ and 2.4 T [expected to be 1.2/cos(60°) T] for $H_{60}{}^\circ$. We normalize the $P_{a^*}(H_{45}{}^\circ)$ data into $P_{a^*}(H_c)$ and combine it with the published $M_c(H_c)$ curve in Fig. 6(d), and the anomalies in $P_{a^*}(H_c)$ precisely coincide with the metamagnetic transitions at ± 1.2 T. The TM induced polarization is nearly linear just below and above the transitions. The tripled dP/dH and magnetization confirm the 1 to 3 TM and M_c change. A maximum ME coefficient $dP/dH = 26.22(6)$ ps/m is obtained at the metamagnetic transition point. Figure 6(e) shows an example of the magnetic structure of a Co triangle sublattice with $TM = +1$ and $M_c = +1$, which is also an object of magnetic chirality. The schematics in Fig. 6(f) shows how the three sublattices evolve with H_c, i.e., "−3 to −1 to 1 to 3" TM and M_c transitions. Clearly, the field-invariant magnetic chirality, which is fixed by global structural chirality, is the essence of $BaCoSiO_4$ to achieve field-tunable TM and ME effect.

Overall, the $BaCoSiO_4$ single crystal shows not only a conventional $H \| P$ type ME effect, but also an exotic $H \perp P$ type TM induced ME effect. These findings strongly suggest that each bulk crystal has a single and invariant magnetic chiral domain, and the monostructural global chirality is possibly the root cause. Note that both global and local chiral structures have very low symmetry and permit nonzero DM interactions. However, the local chiral contribution is supposed to be canceled out due to the multiple domains. Thus, the observed magnetic chirality only couples with the global chirality. In addition, the observed multistep and low-barrier control of magnetization and polarization provides insights into next-generation ME and memory devices.

IV. CONCLUSION

A triangular lattice antiferromagnet $BaCoSiO_4$ single crystal with a chiral and polar crystal structure (RT space group $P6_3$) was synthesized by the LFZ method. We identify diverse ferroic orders of $BaCoSiO_4$ at room temperature and explore their hierarchical phase transitions through domain observations. We discover the formation of Z_3 (anti)vortices driven by a trimerization-type structural instability, the ferrorotational domains from the in-plane distortion of bridging oxygens, and lateral nanosized polar domains limited to the Co^{2+}/Si^{4+} ionic ordering process. Our results reveal a trimerization coupled with the ferrorotational transition at 530 °C instead of a polar-coupled transition, which differs distinctly from other tridymite derivatives, e.g., $BaAl_2O_4$. $BaAl_2O_4$ has been proposed as an improper ferroelectric from the analysis of group theory, in which the primary order parameter M_2 vibration mode is coupled with the secondary Γ_2 polar mode [46]. The decoupling of polar mode and the detailed symmetry analysis in $BaCoSiO_4$ found in this work call for further attention.

Interestingly, two-step chirality develops. We found that the single global chirality possibly locks the single magnetic chirality below 3.2 K, so a net TM can exist and be tunable by an external magnetic field along the c axis. As a result, the magnetic toroidicity induced ME effect has been successfully observed with a maximum ME coefficient of 26.22(6) ps/m. Our results unveil the complex structures and phase transitions, the critical role of domain configuration for macroscopic properties, and the tunable coupling between magnetization and polarization. $BaCoSiO_4$ is a unique playground for studying the multifaceted coupling of structural and magnetic ferroic orders and promising material for next-generation multifunctional electronic devices.

ACKNOWLEDGMENTS

The work at Rutgers University was supported by the DOE under Grant No. DOE: DE-FG02-07ER46382. Experiments performed in the Materials Growth and Measurement Laboratory [47] were supported within the program of Czech Research Infrastructures (Project No. LM2018096). Work at

SNU was supported by the Institute for Basic Science (IBS) in Korea (Grant No. IBS-R009-G1) and the Leading Researcher Program of the National Research Foundation of Korea (Grant No. 2020R1A3B2079375).

[1] S.-W. Cheong, D. Talbayev, V. Kiryukhin, and A. Saxena, Broken symmetries, non-reciprocity, and multiferroicity, npj Quantum Mater. **3**, 19 (2018).

[2] W. Jin, E. Drueke, S. Li, A. Admasu, R. Owen, M. Day, K. Sun, S.-W. Cheong, and L. Zhao, Observation of a ferro-rotational order coupled with second-order nonlinear optical fields, Nat. Phys. **16**, 42 (2020).

[3] A. A. Gorbatsevich and Y. V. Kopaev, Toroidal order in crystals, Ferroelectrics **161**, 321 (1994).

[4] N. A. Spaldin, M. Fiebig, and M. Mostovoy, The toroidal moment in condensed-matter physics and its relation to the magnetoelectric effect, J. Phys.: Condens. Matter **20**, 434203 (2008).

[5] M. J. Buerger, The stuffed derivatives of the silica structures, Am. Mineral. **39**, 600 (1954).

[6] D. D. Nihtianova, I. T. Ivanov, J. J. Macicek, and I. K. Georgieva, Crystallographic data for $BaMnSiO_4$: A new phase in the system BaO-MnO-SiO_2, Powder Diffr. **12**, 167 (1997).

[7] V. Kahlenberg, J. B. Parise, Y. Lee, and A. Tripathi, Characterization of the stuffed framework structures $BaAlGaO_4$ and $BaFeGaO_4$, Z. Kristallogr. - Cryst. Mater. **217**, 249 (2002).

[8] A. M. Abakumov, O. I. Lebedev, L. Nistor, G. V. Tendeloo, and S. Amelinckx, The ferroelectric phase transition in tridymite type $BaAl_2O_4$ studied by electron microscopy, Phase Transitions **71**, 143 (2000).

[9] B. Liu and J. Barbier, Structures of the stuffed tridymite derivatives, Ba$M$$SiO_4$ (M = Co, Zn, Mg), J. Solid State Chem. **102**, 115 (1993).

[10] S. Mori, S. Katsumura, T. Ozaki, E. Tanaka, Y. Ishii, K. Kurushima, Y. Kubota, and H. Taniguchi, Structural Phase transition and microstructures in stuffed tridymite-type compounds; $Ba(Al, Fe)_2O_4$, Ferroelectrics **464**, 116 (2014).

[11] T. Nagai, S. Asai, R. Okazaki, I. Terasaki, and H. Taniguchi, Effects of element substitution on the pyroelectric phase transition of stuffed-tridymite-type $BaZnGeO_4$, Solid State Commun. **219**, 12 (2015).

[12] S.-Y. Huang, R. Von Der Mühll, J. Ravez, J. P. Chaminade, P. Hagenmuller, and M. Couzi, A propos de la ferroeléctricité dans $BaAl_2O_4$, J. Solid State Chem. **109**, 97 (1994).

[13] H. Takei, S. Tsunekawa, and M. Maeda, Growth and properties of $BaZnGeO_4$ crystals, J. Mater. Sci. **15**, 2612 (1980).

[14] H. Taniguchi, H. Moriwake, A. Kuwabara, T. Okamura, T. Yamamoto, R. Okazaki, M. Itoh, and I. Terasaki, Photo-induced change of dielectric response in $BaCoSiO_4$ stuffed tridymite, J. Appl. Phys. **115**, 164103 (2014).

[15] M. Avdeev, S. Yakovlev, A. A. Yaremchenko, and V. V. Kharton, Transitions between $P2_1$, $P6_3$(3A), and $P6_322$ modifications of $SrAl_2O_4$ by *in situ* high-temperature x-ray and neutron diffraction, J. Solid State Chem. **180**, 3535 (2007).

[16] D. den Engelsen, G. R. Fern, T. G. Ireland, and J. Silver, Laser-activated luminescence of $BaAl_2O_4$:Eu, ECS J. Solid State Sci. Technol. **9**, 026001 (2020).

[17] Y. Ishii, S. Mori, Y. Nakahira, C. Moriyoshi, J. Park, B. G. Kim, H. Moriwake, H. Taniguchi, and Y. Kuroiwa, Two competing soft modes and an unusual phase transition in the stuffed tridymite-type oxide $BaAl_2O_4$, Phys. Rev. B **93**, 134108 (2016).

[18] L. Ding *et al.*, Field-tunable toroidal moment in a chiral-lattice magnet, Nat. Commun. **12**, 5339 (2021).

[19] T. Choi, Y. Horibe, H. T. Yi, Y. J. Choi, W. Wu, and S. W. Cheong, Insulating interlocked ferroelectric and structural antiphase domain walls in multiferroic $YMnO_3$, Nat. Mater. **9**, 253 (2010).

[20] D. Grohol, K. Matan, J.-H. Cho, S.-H. Lee, J. W. Lynn, D. G. Nocera, and Y. S. Lee, Spin chirality on a two-dimensional frustrated lattice, Nat. Mater. **4**, 323 (2005).

[21] Y. Ishikawa, K. Tajima, D. Bloch, and M. Roth, Helical spin structure in manganese silicide MnSi, Solid State Commun. **19**, 525 (1976).

[22] S.-W. Cheong, S. Lim, K. Du, and F.-T. Huang, Permutable SOS (symmetry operational similarity), npj Quantum Mater. **6**, 58 (2021).

[23] N. Lee, Y. J. Choi, and S.-W. Cheong, Magnetic control of ferroelectric polarization in a self-formed single magnetoelectric domain of multiferroic $Ba_3NbFe_3Si_2O_{14}$, Appl. Phys. Lett. **104**, 072904 (2014).

[24] S.-W. Cheong, SOS: Symmetry-operational similarity, npj Quantum Mater. **4**, 53 (2019).

[25] J. Rodríguez-Carvajal, Recent advances in magnetic structure determination by neutron powder diffraction, Phys. B (Amsterdam) **192**, 55 (1993).

[26] See Supplemental Material at http://link.aps.org/supplemental/10.1103/PhysRevB.105.184407 for six symmetry-equivalent domains, DSC, temperature evolution of lattice parameters, magnetic susceptibility, raw data of pyroelectric and magnetoelectric current, magnetoelectric coefficient, and field-dependent permittivity.

[27] N. Tanba, M. Wada, and Y. Ishibashi, A new ferroelectric phase in $BaZnGeO_4$, J. Phys. Soc. Jpn. **54**, 4783 (1985).

[28] H. Lemmens, S. Amelinckx, G. Van Tendeloo, A. M. Abakumov, M. G. Rozova, and E. V. Antipov, Transmission electron microscopy study of polymorphism in barium gallate $BaGa_2O_4$, Phase Transitions **76**, 653 (2003).

[29] M. Tanaka and G. Honjo, Electron optical studies of barium titanate single crystal films, J. Phys. Soc. Jpn. **19**, 954 (1964).

[30] R. Gevers, H. Blank, and S. Amelinckx, Extension of the Howie-Whelan equations for electron diffraction to non-centro symmetrical crystals, Phys. Status Solidi B **13**, 449 (1966).

[31] M. Fiebig, Revival of the magnetoelectric effect, J. Phys. D: Appl. Phys. **38**, R123 (2005).

[32] D. N. Astrov, The magnetoelectric effect in antiferromagnetics, J. Exp. Theor. Phys. **11**, 708 (1960).

[33] D. N. Astrov, Magnetoelectric effect in chromium oxide, J. Exp. Theor. Phys. **13**, 729 (1961).

[34] V. J. Folen, G. T. Rado, and E. W. Stalder, Anisotropy of the Magnetoelectric Effect in Cr_2O_3, Phys. Rev. Lett. **6**, 607 (1961).

[35] G. T. Rado and V. J. Folen, Observation of the Magnetically Induced Magnetoelectric Effect and Evidence for Antiferromagnetic Domains, Phys. Rev. Lett. **7**, 310 (1961).

[36] G. T. Rado and J. M. Ferrari, Magnetoelectric effects in $TbPO_4$, in *Magnetism and Magnetic Materials—1972: Eighteenth Annual Conference*, AIP Conf. Proc. No. 10 (AIP, Melville, NY, 1973), p. 1417.

[37] Y. Wang, G. L. Pascut, B. Gao, T. A. Tyson, K. Haule, V. Kiryukhin, and S.-W. Cheong, Unveiling hidden ferrimagnetism and giant magnetoelectricity in polar magnet $Fe_2Mo_3O_8$, Sci. Rep. **5**, 12268 (2015).

[38] Y. S. Oh, S. Artyukhin, J. J. Yang, V. Zapf, J. W. Kim, D. Vanderbilt, and S.-W. Cheong, Non-hysteretic colossal magnetoelectricity in a collinear antiferromagnet, Nat. Commun. **5**, 3201 (2014).

[39] I. Kornev, M. Bichurin, J. P. Rivera, S. Gentil, H. Schmid, A. G. M. Jansen, and P. Wyder, Magnetoelectric properties of $LiCoPO_4$ and $LiNiPO_4$, Phys. Rev. B **62**, 12247 (2000).

[40] A. S. Zimmermann, D. Meier, and M. Fiebig, Ferroic nature of magnetic toroidal order, Nat. Commun. **5**, 4796 (2014).

[41] M. Baum, K. Schmalzl, P. Steffens, A. Hiess, L. P. Regnault, M. Meven, P. Becker, L. Bohatý, and M. Braden, Controlling toroidal moments by crossed electric and magnetic fields, Phys. Rev. B **88**, 024414 (2013).

[42] Y. F. Popov, A. M. Kadomtseva, G. P. Vorob'ev, V. A. Timofeeva, D. M. Ustinin, A. K. Zvezdin, and M. M. Tegeranchi, Magnetoelectric effect and toroidal ordering in $Ga_{2-x}Fe_xO_3$, J. Exp. Theor. Phys. **87**, 146 (1998).

[43] T. Hayashida, K. Kimura, D. Urushihara, T. Asaka, and T. Kimura, Observation of ferrochiral transition induced by an antiferroaxial ordering of antipolar structural units in $Ba(TiO)Cu_4(PO_4)_4$, J. Am. Chem. Soc. **143**, 3638 (2021).

[44] Y. S. Tang, S. M. Wang, L. Lin, Cheng Li, S. H. Zheng, C. F. Li, J. H. Zhang, Z. B. Yan, X. P. Jiang, and J.-M. Liu, Collinear magnetic structure and multiferroicity in the polar magnet $Co_2Mo_3O_8$, Phys. Rev. B **100**, 134112 (2019).

[45] Y. S. Tang, J. H. Zhang, L. Lin, R. Chen, J. F. Wang, S. H. Zheng, C. Li, Y. Y. Zhang, G. Z. Zhou, L. Huang *et al.*, Metamagnetic transitions and magnetoelectricity in the spin-1 honeycomb antiferromagnet $Ni_2Mo_3O_8$, Phys. Rev. B **103**, 014112 (2021).

[46] H. T. Stokes, C. Sadate, D. M. Hatch, L. L. Boyer, and M. J. Mehl, Analysis of the ferroelectric phase transition in $BaAl_2O_4$ by group theoretical methods and first-principles calculations, Phys. Rev. B **65**, 064105 (2002).

[47] http://mgml.eu.